ORIGINAL ARTICLE

Fast-converging robust PR-P controller designed by using symmetrical pole placement method for current control of interleaved buck converter-based PV emulator

Cagfer Yanarates | Zhongfu Zhou

Electrical and Electronic Engineering Department, Swansea University, Swansea, UK

Correspondence
Cagfer Yanarates, Swansea University, Bay Campus, SA1 8EN Swansea, UK.
Emails: cagferyanarates@gmail.com; 887912@swansea.ac.uk

Abstract

In this study, the interleaved buck converter-based photovoltaic (PV) emulator current control is presented. A proportional-resonant-proportional (PR-P) controller is designed to resolve the drawbacks of conventional PI controllers in terms of phase management, which means balancing currents evenly between active phases to avoid thermally stressing and provide optimal ripple cancelation in the presence of parameter uncertainties. The resonant path of the controller (PR) with a constant proportional unity gain is designed considering the changing dynamics of a notch filter by pole placement method (adding mutually complementary poles to the notch transfer function) at PWM switching frequency. The proportional gain path (P) of the controller is used to determine the compatibility of the controller with parameter uncertainty of the phases and designed by utilizing loop-shaping method. The proposed controller shows superior performance in terms of 10 times faster-converging transient response, zero steady-state error with significant reduction in current ripple. Equal load sharing that constitutes the primary concern in multiphase converters is achieved with the proposed controller. Implementing of robust control theory involving comprehensive time and frequency domain analysis reveals 13% improvement in the robust stability margin and 12-degree bigger phase toleration with the PR-P controller. In addition to these, the proposed unconventional design process of the controller reduces the computational complexity and provides cost-effectiveness and simple implementation. Moreover, implementing of auxiliary resistor-capacitor (RC) circuits parallel with the inductors to sense the current in each phase removes the need for current measurement sensors that contribute to overall cost of the system.

KEYWORDS
auxiliary resistor-capacitor (RC) circuit, interleaved buck converter, lossless current sensing, proportional-resonant-proportional (PR-P) current controller, PV emulator (PVE), state-space average modelling

1 | INTRODUCTION

Depletion of fossil fuels and consequential environmental losses of anthropogenic disturbances prognosticate that power generation from renewable energy sources will become more of an issue in future.[1-4]

Many research studies conducted on sustainable energy have shown that solar power with its almost zero detrimental effect on the environment uncontrovertibly is one of the prominent renewable energy sources.[5–8] In addition to its slightest impact on the environment, solar power is the most abundant and inexhaustible source of energy.[9,10] Photovoltaic (PV) panels for solar energy generation have wide range of applications from residential districts to large-scale solar power plants.[11] Another primary advantage of PV system is that extensive maintenance is not required after installation process.[12,13]

PV systems basically consist of PV arrays and power electronic converters.[14] These converters constitute the most essential components of the PV systems due to their use of capturing the maximum power generation from PV arrays and subsequently feeding the generated power into the grid.[15] In this regard, the development of high-efficiency power electronic converters and high-performance maximum power point tracking (MPPT) algorithms are imperative.[16,17] Implemented MPPT algorithms and power electronics converters have to ensure the maximum possible power generation despite the variation of temperature, irradiance, and nonlinear behaviors of solar cells.[18,19]

Testing the performance of the MPPT algorithms and the power electronic converters with real installed solar panels is a considerable challenge because of the constraints such as need for wide surrounding space, high installation cost, and the lack of control over the environmental conditions.[3,20] Under such constraints, the use of PVEs is the most cost-effective solution to test MPPT algorithms and power electronics converters.[7,15] The use of cost-effective emulators provides a clear incentive for global enterprise and scientific development.[21] For the ideal PVE, there are specific requirements, which include a proper emulation of nonlinear I-V and P-V characteristics of a PV panel, which function under varying atmospheric conditions (temperature and irradiance).[16] The emulator must be able to integrate Power Electronics Converter interfaces for testing.[20] It must also be able to function appropriately under frequent load changes.[18] Contemporary scientific enquiry has found that emulated I-V and P-V curves produce similar results to real PV panel outcomes (in terms of the datasheet).[22] However, advantages and disadvantages have been identified in terms of performance criteria, such as implementation costs; efficiency; accuracy; the level of complexity; sensitivity to variable environmental conditions; and frequent load changes.[3,14,23]

In this study, interleaved buck converter-based PVE current control is presented. Compared to single-phase buck regulator based PVE, interleaved buck converter-based PVE offer several advantages such as reduction in both input and output capacitance, improvement in thermal performance and efficiency, and enhancement in overshoot and undershoot during load transients.[24,25] While interleaved buck converter-based PVE provides many benefits, implementing of additional phases pose challenges, for instance, phase management, complexity, increase in the cost of components, and printed-circuit board (PCB) area.[26] The phase management is the most significant major challenge in multiphase converter applications.[27] Achieving the highest potential performance is required to balance current evenly between active phases to avoid thermal stress in each phase and ensure optimal ripple cancelation.[28,29] Moreover, addition and removing of each phase quickly during transients matters a great deal for minimizing excursions on the output voltage. Considering all these reasons, yielding optimum efficiency from the multiphase buck converter-based PVE leads to the necessity to develop more sophisticated control strategies. The comparative analysis of the most common developed control techniques for multiphase converter applications in terms of their features, advantages, and limitations is given in Table 1.

The paper proposes a novel and unprecedented Proportional-Resonant-Proportional (PR-P) controller designed by symmetrical poles placement method together with use of robust control theory for the current control of interleaved buck converter-based PVE. The proposed controller shows superior performance in terms of fast-converging transient response, zero steady-state error, significant reduction in current ripple, and properly functioning with parameters uncertainty (highly robust) that constitutes primary concern in multiphase converters' load sharing. For the purpose of verification and validation of the designed controller, a comparative analysis with a PI controller is also presented to illustrate the efficiency of the proposed control scheme. In addition to improved dynamics of the control process, unconventional design process of the controller reduces the computational complexity and provides cost-effectiveness and simple implementation. Moreover, implementing of auxiliary Resistor-Capacitor (RC) circuits parallel with the inductors to sense the current in each phase removes the need for current measurement sensors that contribute to overall cost of the system.

TABLE 1 Characteristics of commonly used control techniques for multiphase converter applications

Control technique	Features	Advantages	Limitations	References
Proportional-integral (PI)	• Suitable for linear control • Low-complexity	• Simple implementation • Fast transient response • Easy integration with various control techniques	• Incapable of responding to external disturbance (eg, load variations) • High settling time, steady-state error, overshoots	[30–34]
Sliding mode control (SMC)	• Robust and suitable for nonlinear control • Converge toward sliding surface	• Simple implementation • Capable of responding to external disturbance • Fast dynamics (eg, settling time) • Robust	• Chattering issues due to discontinuous control law • Excessive overshoots	[31,34–38]
Model predictive control (MPC)	• Easy for online iteration • Robust and suitable for nonlinear control • Enable to predict future states	• Enhanced transient performance with external constraints • Fast response • Efficient tracking with estimation-based techniques	• Sensitive to circuit parameters • High computational burden • Required for detailed knowledge of the model	[30,34,39–41]
State-space modeling (SSM)	• Robust and suitable for nonlinear control • Suitable for multiple-input and multiple-output systems • Enable to estimate plant states continuously	• Improved transient response • Less overshoot during load varying conditions	• Required for longer period of time for initial implementation • Required for detailed knowledge of the model	[34,42–45]
Fuzzy logic control (FLC)	• Robust and suitable for nonlinear control • Providing stability in the presence of large variations • Suitable for the systems presenting imprecise boundary conditions	• Less overshoots • Efficient tracking response • Do not require the mathematical of the plant	• High computational burden • Required for properly defined rules for operation • Longer settling time	[34,46–49]

2 | PROPOSED PR-P CONTROLLER DESIGN

The proposed PR-P controller consists of two parts: one part is Proportional-Resonant (PR), which constitutes resonant path of the controller with a constant proportional unity gain, and the other part is proportional gain (P), which is used to determine the compatibility of the controller with parameters of the plant in question to accomplish optimum efficiency.[50] Figure 1 shows circuit diagram of PR-P current control of interleaved buck converter (two buck converters connected in parallel)-based PVE. Control scheme of the overall system consists of two PR-P controllers for current control in each phase and one PI controller to ensure the current balance (equal load sharing) between phases, mathematical model of the emulated PV panel for the generation of the reference current under varying temperature and irradiance values. Determining the phase currents is done by utilizing the parasitic DC resistances of the inductors by integration of auxiliary Resistor-Capacitor (RC) circuits parallel to the inductors in each phase.

The PR component of the controller is designed by considering the changing dynamics of a notch filter with the addition of mutually complementary poles to the notch transfer function whose resonant frequency is PWM switching frequency of the buck converter.

Transfer function of the ideal PR controller is represented by:

$$G_{PR}(s) = K_P + K_I \frac{s}{s^2 + \omega_r^2} \tag{1}$$

where K_P, K_I, and ω_r are proportional gain, integral gain, and resonant frequency, respectively. Frequency response of the ideal transfer function of the PR controller indicates formation of a phase shift and an infinite gain. The attained infinite gain leads to zero steady-state error and occurs only at the resonant frequency (ω_r). Setting the resonant frequency at any specified value enables to track periodic signals efficiently and error-free. However, practical applications of the ideal PR controller reveal stability issues resulting from the infinite gain generation at the resonant frequency.[51] Resolution of stability problem is managed with
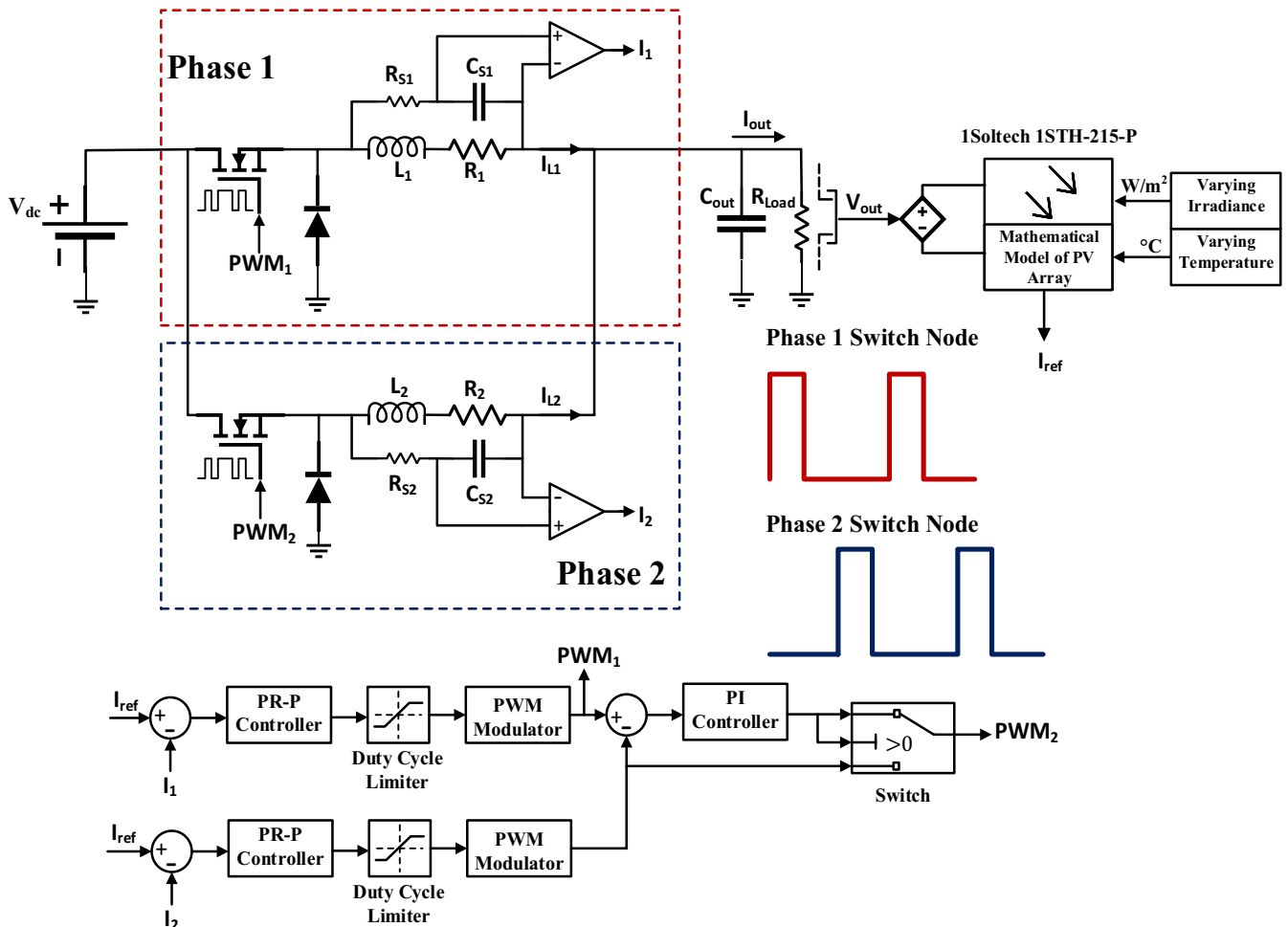

FIGURE 1 PR-P current control of interleaved buck converter

implementing of a non-ideal PR controller. The non-ideal PR controller is derived by introducing damping to the ideal transfer function.[52,53] The non-ideal PR controller transfer function with addition of the bandwidth (ω_c) around the ac resonant frequency (ω_r) is represented by:

$$G_{PR}(s) = K_P + K_I \frac{2\omega_c s}{s^2 + 2\omega_c s + \omega_r^2} \quad (2)$$

While the ideal PR controller generates an infinite gain at the resonant frequency ω_r, the non-ideal PR controller's gain is finite that still measures up the sufficient magnitude for sorting out the steady-state error with almost zero outcome.[53] General representation of magnitude response of a notch filter and a PR controller in decibels (dB) versus frequency is given in Figure 2. Resonant path of the proportional resonant (PR) controller is a notch filter that can be described with three basic identifications as depth of the notch, resonant frequency, and width of the notch. The PR path of the proposed PR-P controller in the study is designed based on altering the notch filter dynamics and subsequently taking the reciprocal of the generated notch filter transfer function at the switching frequency of the buck converter. The proposed notch filter design process containing applied parameters and their functions is given in Figure 3.

The effects of variations in the damping ratio (ξ) and the parameter k on frequency response of the notch characterized by magnitude and phase responses are given in Figure 4. The parameter k is set to adjust the width of the notch, the damping ratio (ξ) is set to adjust the depth of the notch, and the natural frequency (ω_n) is set to adjust the location of the notch that refers to resonant frequency for the PR path of the proposed PR-P controller.

The variable k will be defined as the ratio of each pole located on both sides of the natural frequency that determines cutoff frequencies of the complementary poles. The parameter k can be adjusted according to the requirement. The larger value of k corresponds with a wider notch, and vice versa.

An unrealizable transfer function $G(s)$ that is lightly damped ($\xi = 0.0001$) pair of zeros centered at the PWM switching frequency of the buck converter ($\omega_n = 10$ kHz) that corresponds to the resonant frequency of the PR and the k ($k = 2$) for the application is given by:

$$G(s) = \frac{s^2 + 2\xi\omega_n s + \omega_n^2}{\omega_n^2} \quad (3)$$

First pole s_1 with a cutoff frequency k time larger than the natural frequency is given by:

$$s_1 = \frac{k\omega_n}{s + k\omega_n} \quad (4)$$

Second pole s_2 with a cutoff frequency k time smaller than the natural frequency is given by:

$$s_2 = \frac{\frac{\omega_n}{k}}{s + \frac{\omega_n}{k}} \quad (5)$$

Addition of both poles s_1 and s_2 to the transfer function $G(s)$ results in a formation of a second-order band-stop filter whose transfer function $G_{notch}(s)$ is given by:

$$G_{notch}(s) = G(s) \cdot s_1 \cdot s_2 = \frac{s^2 + 2\xi\omega_n s + \omega_n^2}{\omega_n^2} \cdot \frac{k\omega_n}{s + k\omega_n} \cdot \frac{\frac{\omega_n}{k}}{s + \frac{\omega_n}{k}} \quad (6)$$

Figure 5A shows the frequency response of the physically unrealizable transfer function of which order of numerator is greater than denominator given in Equation (3). There is a gain rising at 40 dB/decade since there are two unanswered zeros, and thus, the high-frequency signals are to pass through altered. Figure 5B shows that the addition of a pole with a cutoff frequency that is k times larger than the natural frequency dragged the high-frequency magnitude down by 20 dB/decade. Figure 5C shows that addition of a complementary pole with a cutoff frequency that is k times smaller than the natural frequency bended down the high-frequency magnitude by 20 dB/decade to the zero dB.

The transfer function of PR path of the proposed PR-P controller $G_{PR}(s)$ is the reciprocal of the notch filter transfer function $G_{notch}(s)$ is presented as:

$$G_{PR}(s) = \frac{1}{G_{notch}(s)} = \frac{1}{G(s) \cdot s_1 \cdot s_2} = \frac{\omega_n^2}{s^2 + 2\xi\omega_n s + \omega_n^2} \cdot \frac{s + k\omega_n}{k\omega_n} \cdot \frac{s + \frac{\omega_n}{k}}{\frac{\omega_n}{k}} \quad (7)$$

$$G_{PR}(s) = \frac{3.948e09s^2 + 6.201e14s + 1.559e19}{3.948e09s^2 + 4.961e10s + 1.559e19} \quad (8)$$

Addition of the proportional gain K_{P2} to the PR path puts the proposed controller into final form as:

$$G_{PRP}(s) = K_{P2} + G_{PR}(s) = \frac{3.987e11s^2 + 6.251e14s + 1.574e21}{3.948e09s^2 + 4.961e10s + 1.559e19} \quad (9)$$

The magnitude and phase responses of the designed PR-P controller are given in Figure 6. The highest gain of the designed PR-P controller is 82 dB, and it occurs

at the PWM switching frequency of the buck converter ($\omega_n = 10\,kHz$). The phase response shows that the phase shift is zero for low and high frequencies.

Figure 7 shows the unity feedback control structure of the interleaved buck converter PVE with the proposed
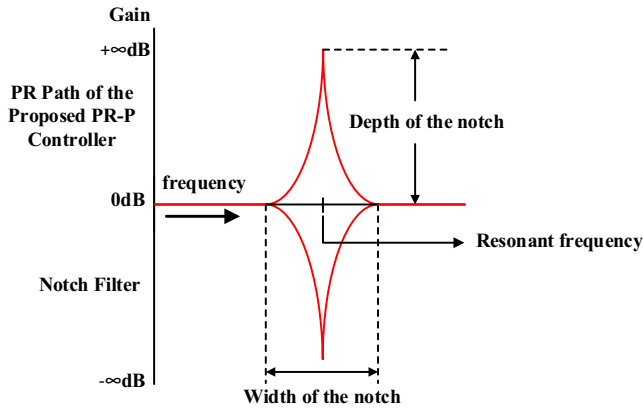

FIGURE 2 Notch filter and PR path of the PR-P controller magnitude response in general form

PR-P controller in s-domain from feedback error (e) to control input (u) to the plant.[19,50]

Continuous transfer function mode of a controller represents the function of each parameter used in the design of the controller. Figure 8 shows the unity feedback control structure of the proposed PR-P controller in continuous transfer function mode from feedback error (e) to control input (u) to the plant.[19,50]

2.1 | Current sensing with auxiliary RC circuit

One of the problems in multiphase converter topologies is the possibility of imbalance between phase currents.[24] If the currents are not in balance, there will not be good cancelation in ripple currents and the amount of power loss in each phase will be different from each other.[54] To assure load balancing, current sensing and feedback are required. In this study, auxiliary RC circuit connected parallel to the inductors in each
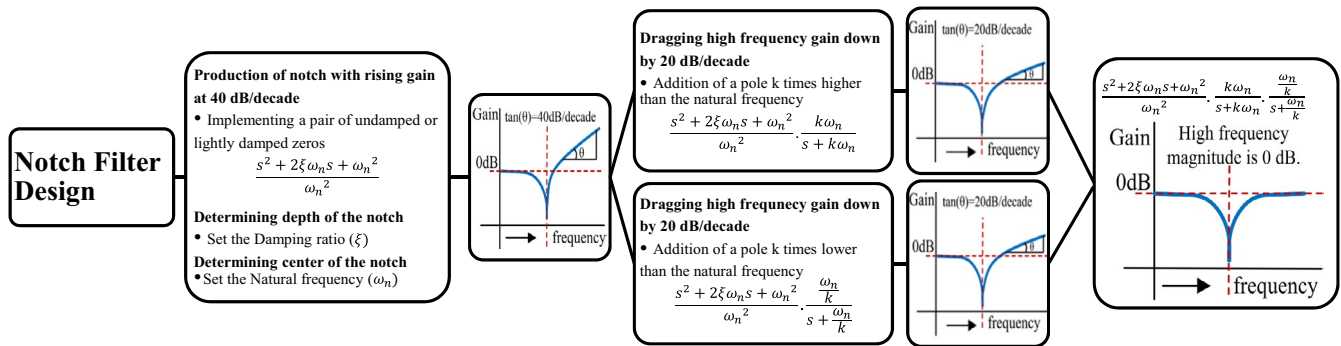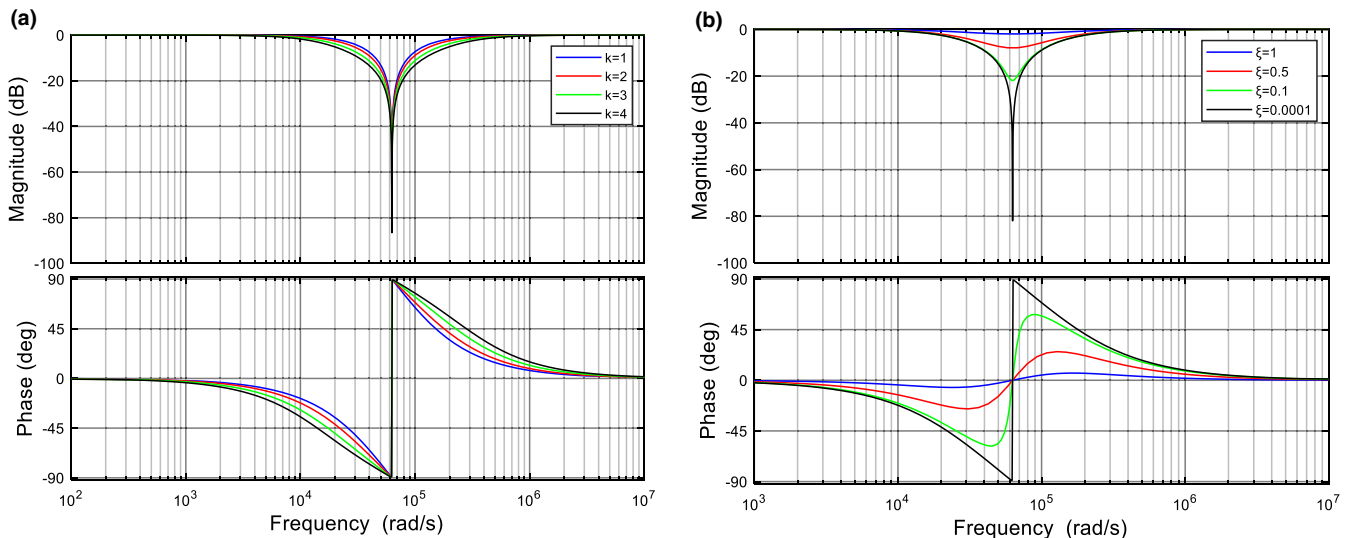

FIGURE 3 Notch filter design process

FIGURE 4 Phase and magnitude response of the notch filter (a) with varying k and (b) with varying ξ
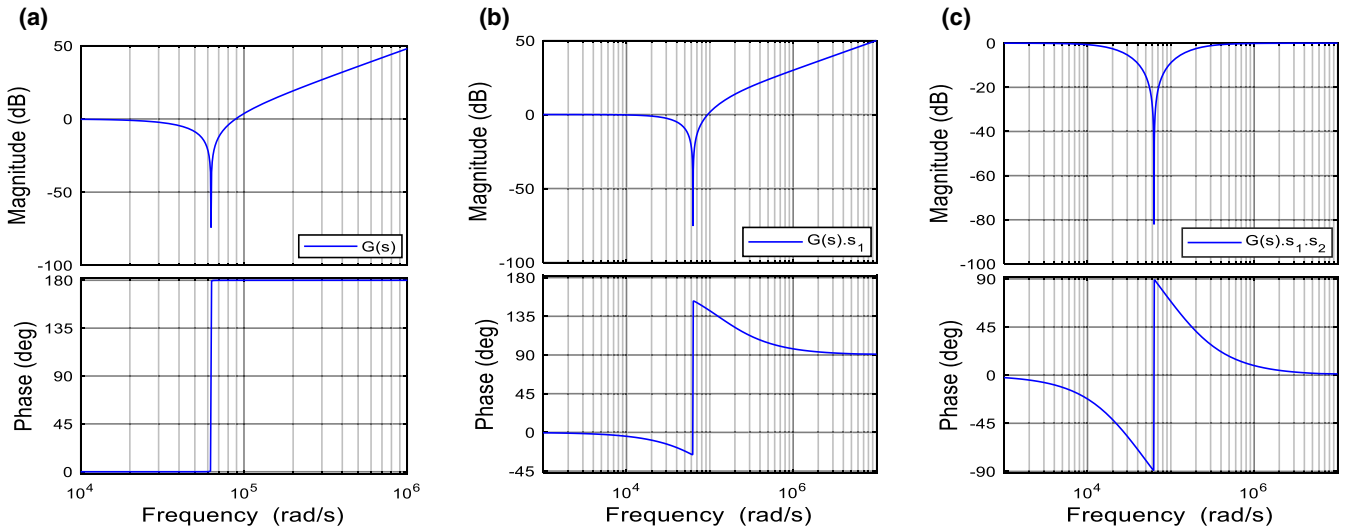
FIGURE 5 The notch filter dynamics-based PR controller. (a) Lightly damped unrealizable transfer function. (b) Addition the first pole. (c) Addition the second complementary pole
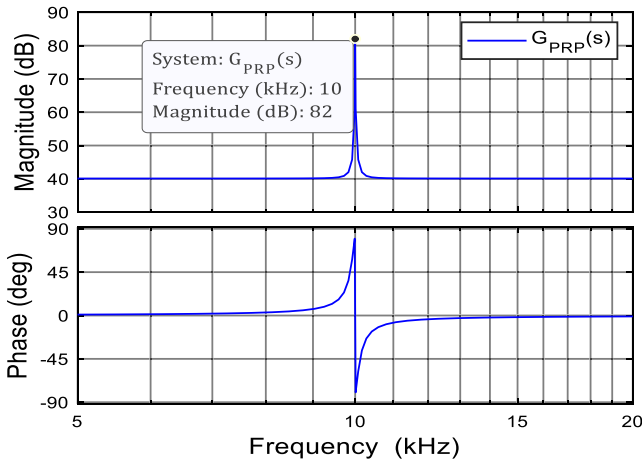

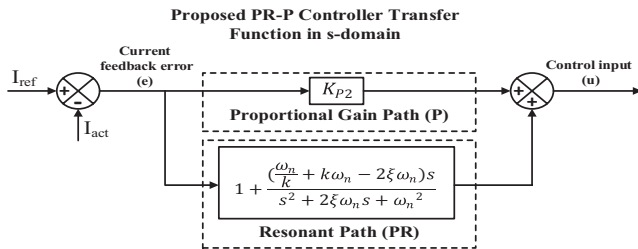**FIGURE 6** Magnitude and phase response of the proposed PR-P controller

FIGURE 7 Unity feedback of PR-P controller in s-domain

FIGURE 8 Unity feedback of PR-P controller in continuous transfer function mode

phase is used for measuring the currents. Accordingly, Figure 9 shows the current sensing part of the phase-1 circuit.

The idea behind this method is utilizing the parasitic resistance of wires of the inductor. There is a voltage drop on the inner parasitic resistance R_1 of the inductor and curr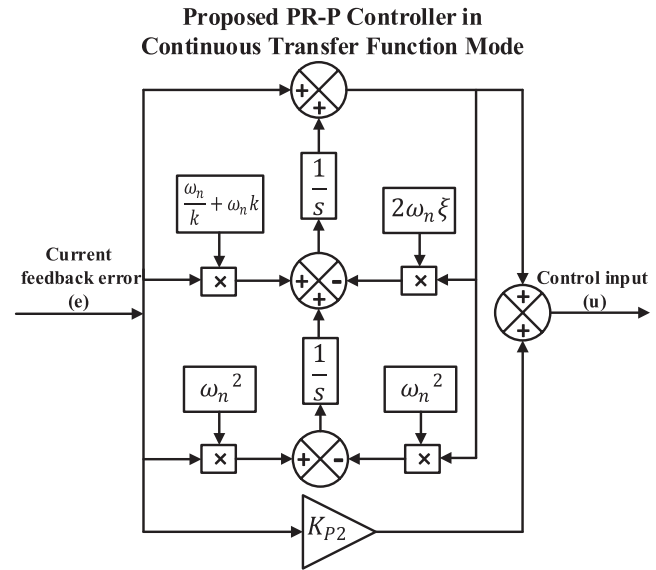ent I_{L1} flowing through the inductor is measured based on this voltage drop. There is no access to R_1, so the measurement is carried out outside with the implementation of RC auxiliary circuit. The voltage V_{S1} across the capacitor C_{S1} is proportional to the R_1, and therefore, it is also proportional to the I_{L1}. Considering the DC situation, voltage drop of the inductor due to its inductance is zero. DC voltage on the parasitic resistance is the DC current times the resistance and accordingly V_{S1} can be written as:

$$V_{S1(DC)} = I_{L1(DC)}R_1 \qquad (10)$$

where $V_{S1(DC)}$ and $I_{L1(DC)}$ are DC voltage and DC current, respectively. Considering the AC

situation (high-frequency components-ripple) with the assumption that most of the current flow through the inductor since impedance of the inductor is much lower than the auxiliary RC circuit (very large resistance), voltage drop on the parasitic resistance is proportional to the inductor current. Therefore, V_{S1} can be written as:

$$V_{S1(AC)} = I_{L1(AC)} \left(R_1 + sL_1 \right) \frac{\frac{1}{sC_{S1}}}{R_{S1} + \frac{1}{sC_{S1}}} \quad (11)$$

where $V_{S1(AC)}$, $I_{L1(AC)}$, $(R_1 + sL_1)$ and $(1/sC_{S1})/(R_{S1} + 1/sC_{S1})$ are AC voltage, AC current, Laplace presentation of impedance of the inductor branch and RC circuit as a voltage divider, respectively. Working the Equation (11) out yields:

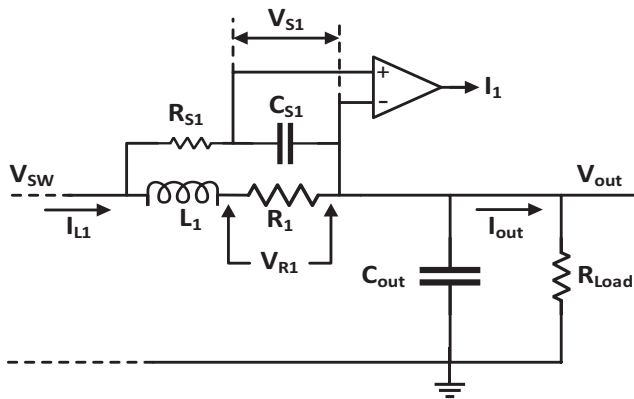$$V_{S1(AC)} = I_{L1(AC)} R_1 \left(\frac{1 + \frac{sL_1}{R_1}}{1 + sC_{S1}R_{S1}} \right) \quad (12)$$

FIGURE 9 Lossless current sensing by using auxiliary RC circuit in parallel with the inductor

If the time constant of the inductor (L_1/R_1) and the RC circuit time constant $(C_{S1}R_{S1})$ are made equal, the voltage across the capacitor is AC current times the parasitic resistance and it can be written as

$$V_{S1(AC)} = I_{L1(AC)}R_1 \quad (13)$$

The Equations (10) and (13) show that the voltage across the capacitor is representing the current flowing through the inductor in both DC and AC situations. Given the inductance value $L_1 = 7.8108e - 04\,\text{H}$, winding resistance value $R_1 = 0.5\Omega$, and arbitrarily selecting a value for $C_{S1} = 1.0414e - 05$, calculation the value of R_{S1} is carried out by setting the time constants of inductor (L_1/R_1) and capacitor $(C_{S1}R_{S1})$ branches equal to each other as follows

$$R_{S1} = \frac{L_1}{R_1} \times \frac{1}{C_{S1}} = 150\Omega \quad (14)$$

The waveforms of actual current and sensed current with amplifier gain of 2 for single-phase buck converter are given in Figure 10.

3 | STATE-SPACE AVERAGE MODELING OF SWITCH MODE POWER SUPPLIES

Analysis of a plant requires developing a mathematical input-output model that best approximates a system's physical reality. A method of constructing a mathematical description of a system is referred to as system modeling. A properly modeled system enables to predict plant response and to observe its behaviors in both time and frequency domains. Transfer function of a plant defines the relation between the output and the input of the system and provides a lot of information about the dynamics of
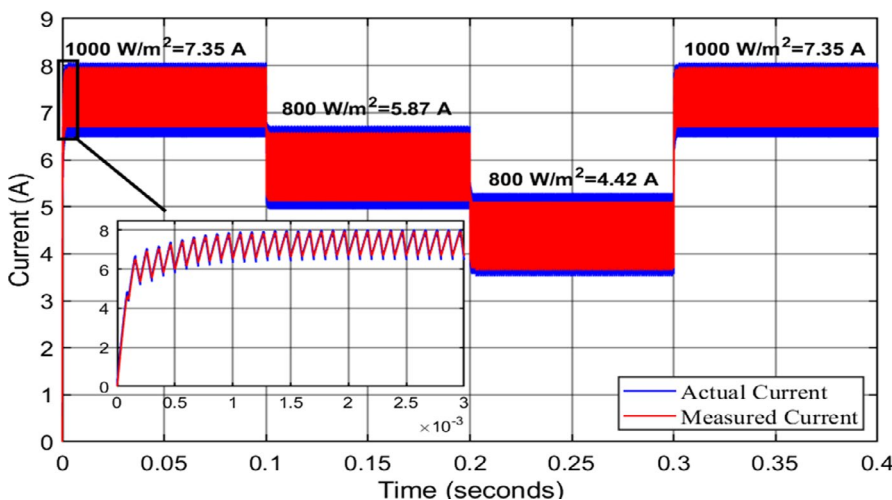

FIGURE 10 RC circuit measured current and actual current

the plant. Furthermore, precisely derived transfer function of a system has great importance for an effective controller design. Control systems are designed and implemented to improve important dynamic properties of the plant such as stability, speed of response, steady-state error, oscillations which constitute the transient and the steady-state responses of the system.[55]

Transfer function model of the intended buck converter is derived by using dynamic (AC small signal) state-space technique.[56,57] This process includes taking the Laplace Transform (with zero initial condition) of both the state and output equations in the state-space model of the buck converter.[58] The most general state-space representation of a system with p inputs, q outputs and n state variables is given in Figure 11. In Figure 11, $x(.)$, $y(.)$, $u(.)$, $A(.)$, $B(.)$, $C(.)$, and $D(.)$ are state vector with $x(t) \in \mathbb{R}^n$, output vector with $y(t) \in \mathbb{R}^q$, input (control) vector with $u(t) \in \mathbb{R}^p$, state (system) matrix with $dim[A(.)] = n \times n$, input matrix with $dim[B(.)] = n \times p$, output matrix with $dim[C(.)] = q \times n$, and feedthrough (feedforward) matrix with $dim[D(.)] = q \times p$, respectively. The flowchart of the state-space averaging technique is given in Figure 12.

State-space average method is one of the developed techniques to obtain the transfer function of the plant and analyze properties and behaviors of the switch mode power supplies (SMPS).[45,58] Providing a substantial insight and its simplicity for both derivation and implementation has made the method a very useful and convenient tool in the applications of power electronics devices.[58,59] The outline of the modeling is summarized in Figure 12. There

are two states determined according to ON-and-OFF the transistor in the circuit, so SMPS circuit analysis consists of two topologies. Description of operating range (intervals) for each state has been made by commonly used conversions and notations as the following:

$$
\begin{aligned}
d &\equiv \text{duty ratio} \\
d' &\equiv 1 - d \\
T_s &\equiv \text{switching period}
\end{aligned}
\tag{15}
$$

A linear-time-invariant (LTI) system model in the tatespace form can be represented as[56]:

$$
\begin{aligned}
\dot{x} &= Ax + Bu \\
y &= Cx + Du
\end{aligned}
\tag{16}
$$

Each state of the SMPS can be described as a set of linear-time-invariant differential equations. The state and output equation for the ON-state during the interval of dT_s is:

$$
\begin{aligned}
\dot{x} &= A_1 x + B_1 v_{in} \\
y_1 &= C_1 x
\end{aligned}
\tag{17}
$$

The state and output equation for the OFF-state during the interval of $d'T_s$ is:

$$
\begin{aligned}
\dot{x} &= A_2 x + B_2 v_{in} \\
y_2 &= C_2 x
\end{aligned}
\tag{18}
$$

The elements of the state vector x are inductor current and capacitor voltage as inductor and capacitor are the only energy storage components of the SMPS. To obtain a single continuous state-space equation (single matrix differential equation), Equations (17) and (18) must be combined in a sense of averaging the system, input and output matrices to result in A, B, and C matrices. The averaging process purely depends on the duty ratio (d) and it is executed as:
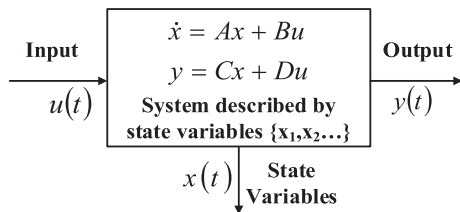

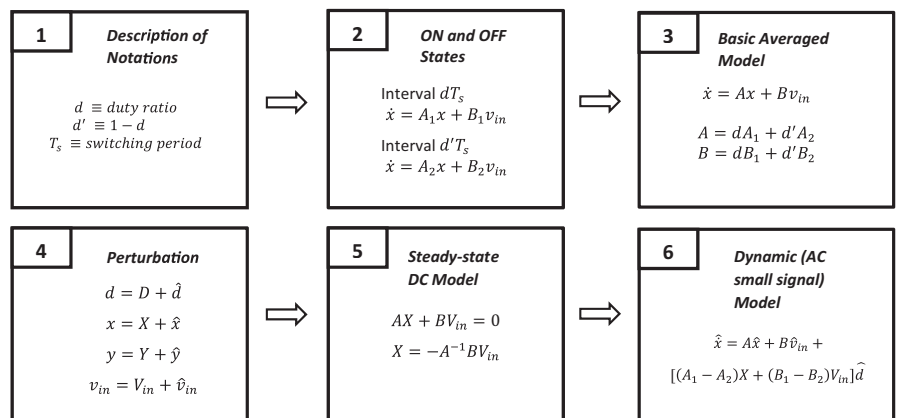**FIGURE 11** The general state-space representation
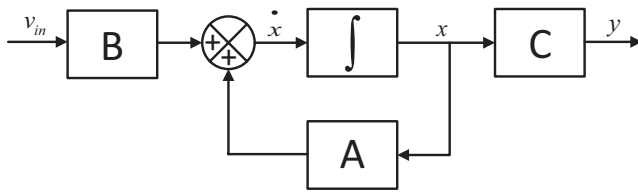

FIGURE 12 Flowchart of state-space averaging method

FIGURE 13 Linear system state-space vector diagram

$$A = dA_1 + d'A_2$$
$$B = dB_1 + d'B_2 \quad (19)$$
$$C = dC_1 + d'C_2$$

The vector block diagram for a linear-time-invariant system in terms of state-space dynamics is given in Figure 13, and the average state-space equation of the system is given in Equation (20).

$$\dot{x} = Ax + Bv_{\text{in}}$$
$$y = Cx \quad (20)$$

The Equation (20) describes the averaged behavior of the SMPS, and it basically removes ripples of the inductor current and capacitor voltage that are the inherent property of the state variables. One of the significant points to note here is that the system matrix A and the input matrix B may be duty ratio dependent, which leads to the conclusion that the averaged equation may be nonlinear regarding the duty ratio (d). The purpose of using state-space model of the SMPS is to generate an equivalent circuit model and carrying out the analysis of the system around a linearization point by perturbing the averaged equation about this operation point. Small signal variation with the steady-state values is represented as:

$$d = D + \hat{d}$$
$$x = X + \hat{x}$$
$$y = Y + \hat{y} \quad (21)$$
$$v_{\text{in}} = V_{\text{in}} + \hat{v}_{\text{in}}$$

The capitalized quantities in Equation (21) represent the steady-state values and the carets are small perturbations. The perturbation is performed by making substitution Equation (21) into Equation (20), and the expanding of the new state-space equation is obtained as the following:

The equation of steady-state operating point when the small signal perturbations are zero is:

$$0 = AX + BV_{\text{in}}$$
$$Y = CX \quad (23)$$

Discarding of the second-order small signal variation terms in Equation (22) results in AC small signal (dynamic) model of the system as the following:

$$\hat{\dot{x}} = A\hat{x} + B\hat{v}_{\text{in}} + \left[(A_1 - A_2)X + (B_1 - B_2)V_{\text{in}}\right]\hat{d}$$
$$\hat{y} = C\hat{x} + (C_1 - C_2)X\hat{d} \quad (24)$$

A, B, and C matrices in Equation (24) are:

$$A = DA_1 + D'A_2$$
$$B = DB_1 + D'B_2 \quad (25)$$
$$C = DC_1 + D'C_2$$

Setting $\hat{v}_{\text{in}} = 0$ produces the response to the variation of the duty factor and the Equation (24) transforms into the following equation:

$$\hat{\dot{x}} = A\hat{x} + \left[(A_1 - A_2)X + (B_1 - B_2)V_{\text{in}}\right]\hat{d}$$
$$\hat{y} = C\hat{x} + (C_1 - C_2)X\hat{d} \quad (26)$$

The simplified representation of the state equation in Equation (26) is:

$$\hat{\dot{x}} = A\hat{x} + F\hat{d} \quad (27)$$

Variation of state variables to the duty factor can be easily solved by application of the Laplace Transform as the following:

$$\frac{\hat{x}}{\hat{d}} = [sI - A]^{-1}F \quad (28)$$

In Equation (28), notation I stands for the unit matrix that is the same size of the system matrix A and $[sI - A]^{-1}$ is the inverse of the matrix $[sI - A]$.

Thus far, the state-space modeling of the DC-to-DC switch mode power converters is represented in terms of small-signal and low-frequency behavior by deriving an equivalent linear circuit description comprising of averaging, perturbation, and linearization process.

$$\dot{X} + \dot{x} = \left[\left(D + \hat{d}\right)A_1 + \left(1 - D - \hat{d}\right)A_2\right](X + \hat{x}) + \left[\left(D + \hat{d}\right)B_1 + \left(1 - D - \hat{d}\right)B_2\right](V_{\text{in}} + \hat{v}_{\text{in}})$$
$$Y + \hat{y} = \left[\left(D + \hat{d}\right)C_1 + \left(1 - D - \hat{d}\right)C_2\right](X + \hat{x}) \quad (22)$$

4 | EMULATED PV PANEL PARAMETERS AND SPECIFICATIONS

Electric characteristics of a PV module are represented graphically by using I-V and P-V characteristics curves. These curves summarize the current-voltage and power-voltage relationships at present conditions of irradiance and temperature of a PV panel. Formation of the curves pertains to PV module's parameters. The emulated PV module is 1Soltech 1STH-215-P with parameter given in Table 2.

Figure 14 shows I-V and P-V curves of the emulated PV panel at 25°C and specified irradiances of 1000, 800, and 600 W/m^2.

The proposed interleaved buck converter-based PVE and its control structure block diagram is given in Figure 1. It takes an input voltage (V_{dc}) of 48 V and converts it into an output voltage of 29 V. The switching frequency is 10 kHz. The minimum load resistance R_{min} is 3.9465 Ω (corresponds to the maximum load condition). In the continuous conduction mode (CCM) operation of the PVE, the maximum ripple allowed in the inductor is 20% of the average inductor current and the maximum load. The maximum ripple in the capacitor is plus and minus 2% of the average output voltage.

4.1 | Calculations the values of buck converter-based PVE components

Buck converter is a switch topology that takes a DC input voltage V_{in} and transforms it to the DC output voltage V_{out}. The output voltage is always smaller than the input voltage ($V_{out} < V_{in}$). In an asynchronous buck converter, the lower switch is implemented by using a diode which will automatically turn on when the upper switch implemented by using a MOSFET or IGBT is turned off. Usually an asynchronous buck converter is designed to operate in CCM in which the operation range is selected in a way that all times the inductor current is positive, which

TABLE 2 The emulated PV module (1Soltech 1STH-215-P) parameters

Parameter	Value
Maximum power (W)	231.15
Open circuit voltage V_{OC} (V)	36.3
Voltage at maximum power point V_{MPP} (V)	29
Temperature coefficient of V_{OC} (% /°C)	−0.36099
Cells per module (Ncell)	60
Short-circuit current I_{SC} (A)	7.84
Current at maximum power point I_{MPP} (A)	7.35
Temperature coefficient of I_{SC}(% /°C)	0.102

ensures that the diode is in forward bias. If this condition is not met the equations that describe the behavior of the converter changes. The switched topology in CCM has two different states shown in Figure 15. When the control signal is high the controllable switch (S) turns on and connects the input voltage to the LC circuit driving the inductor current. This is maintained during a certain amount of time called the on-time t_{on} after which the control signal is changed to a low state which causese the controllable switch to turn off and the current is driven throuhg the diode. This is maintained during a certain amount of time called off-time t_{off}.

The steady-state duty cycle of the plant is represented by:

$$D = \frac{V_{out}}{V_{in}} \qquad (29)$$

The maximum average inductor current is represented by:

$$I_{L,avg,max} = \frac{V_{out}}{R_{min}} \qquad (30)$$

The maximum average inductor ripple current is the 20% of the average current that is represented by:

$$\Delta I_L = 0.2 \times I_{L,avg,max} \qquad (31)$$

Inductance value L of the inductor is represented by:

$$L = \frac{V_{in}(1-D)D}{f_{sw}\Delta I_L} \qquad (32)$$

Capacitor ΔV_C or output voltage ripple ΔV_{out} is the ± 2% of the average output voltage is represented by:

$$\Delta V_C = \Delta V_{out} = 0.04 \times V_{out} \qquad (33)$$

Capacitance value C of the capacitor is represented by:

$$C = \frac{V_{in}(1-D)D}{8Lf_{sw}^2\Delta V_C} \qquad (34)$$

The calculated values of the PVE parameters and components are given in Table 3.

4.2 | Deriving transfer function of the buck converter-based PVE

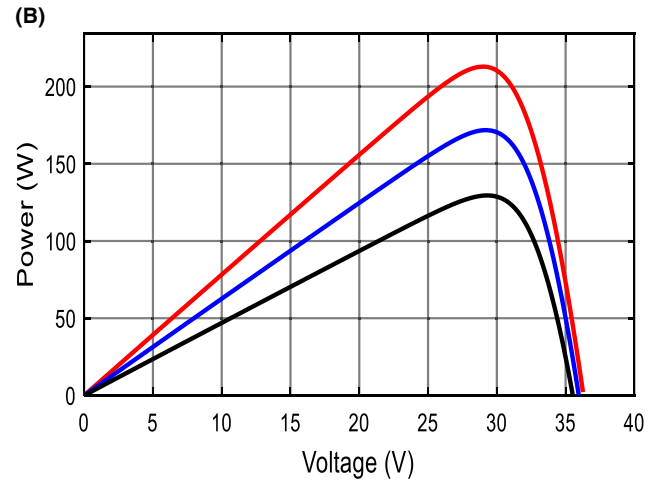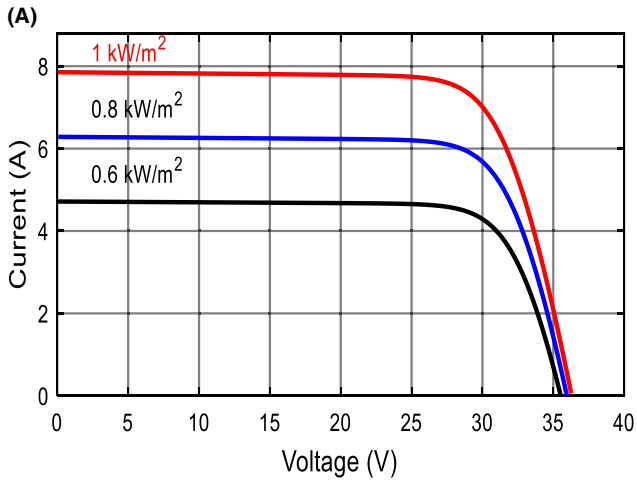Step-by-step transfer function derivation process of the buck converter with its components which are input

(A)

(B)

FIGURE 14 Emulated PV panel characteristics curves (A) I-V curve (B) P-V curve

(A) The on-state (time interval: $0<t<dT_s$)

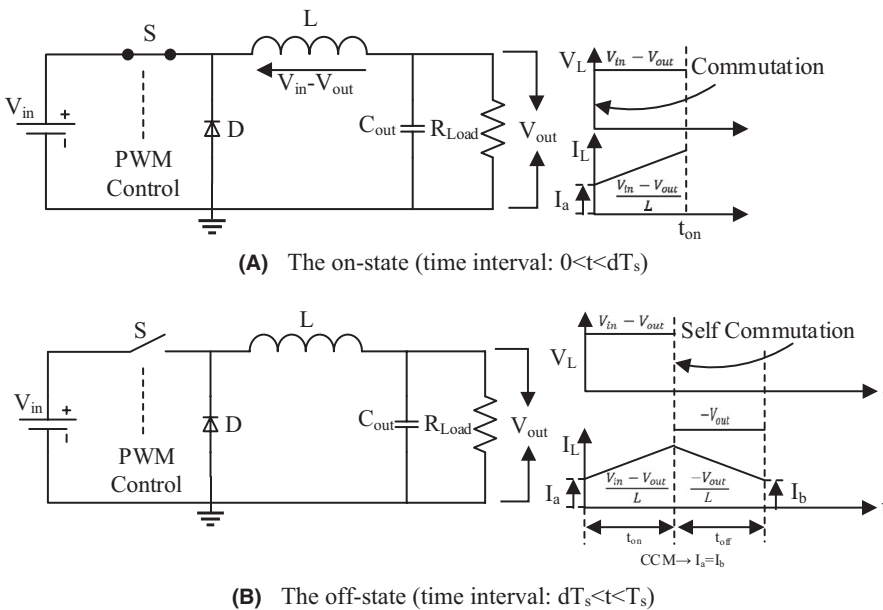**(B)** The off-state (time interval: $dT_s<t<T_s$)

FIGURE 15 The switch topologies and inductor current-voltage waveforms in CCM

TABLE 3 Calculated values of the PVE parameters and components

Parameters and components	Value
Steady-state duty cycle (D)	0.6042
Maximum average inductor current (A)	7.3483
Maximum average inductor current ripple (A)	1.4697
Inductor value (mH)	0.781
Output voltage ripple (V)	1.16
Capacitor value (μF)	15.837

voltage V_{in}, inductance L, output capacitance C_{out}, load resistance R_{Load}, inductor current i_L, capacitor current i_C, inductor voltage V_L, capacitor voltage V_C, steady-state duty cycle D and small signal duty cycle d is presented with the following equations based on comprehensive and systematic analysis of the averaging-perturbation-linearization process of the SMPS explained in Section 3.

Taking Laplace transform of state and output equations with zero initial condition:

$$sX(s) = AX(s) + BU(s)$$
$$Y(s) = CX(s) + DU(s) \quad (35)$$

Rewriting the state equation as:

$$sX(s) - AX(s) = BU(s)$$
$$(sI - A)X(s) = BU(s) \quad (36)$$

By premultiplying $(sI - A)^{-1}$ to both sides of the Equation (36) yields:

$$X(s) = (sI - A)^{-1} BU(s) \quad (37)$$

TABLE 4 Calculated values of the PVE parameters and components

	On-state (time interval: $0 < t < dT_s$)	Off-state (time interval: $dT_s < t < T_s$)	State-space averaging
Derivation of state equations	$V_L = L\frac{di_L}{dt} = V_{in} - V_{out}$ $\frac{di_L}{dt} = \frac{V_{in} - V_{out}}{L}$ $i_L = i_{out} + i_C$ $i_L = \frac{V_{out}}{R_{Load}} + C_{out}\frac{dV_C}{dt}$ $\frac{dV_C}{dt} = \frac{i_L}{C_{out}} - \frac{V_{out}}{R_{Load}C_{out}}$	$V_L = L\frac{di_L}{dt} = -V_{out}$ $\frac{di_L}{dt} = \frac{-V_{out}}{L}$ $i_L = i_{out} + i_C$ $i_L = \frac{V_{out}}{R_{Load}} + C_{out}\frac{dV_C}{dt}$ $\frac{dV_C}{dt} = \frac{i_L}{C_{out}} - \frac{V_{out}}{R_{Load}C_{out}}$	The averaged system matrix $A = \begin{bmatrix} 0 & \frac{-1}{L} \\ \frac{1}{C_{out}} & \frac{-1}{RC_{out}} \end{bmatrix}$
System matrices	$A_1 = \begin{bmatrix} 0 & \frac{-1}{L} \\ \frac{1}{C_{out}} & \frac{-1}{RC_{out}} \end{bmatrix}$	$A_2 = \begin{bmatrix} 0 & \frac{-1}{L} \\ \frac{1}{C_{out}} & \frac{-1}{RC_{out}} \end{bmatrix}$	The averaged input matrix $B = \begin{bmatrix} \frac{D}{L} \\ 0 \end{bmatrix}$
Input matrices	$B_1 = \begin{bmatrix} \frac{1}{L} \\ 0 \end{bmatrix}$	$B_2 = \begin{bmatrix} 0 \\ 0 \end{bmatrix}$	Averaged state-space equation $\dot{x} = Ax + BV_{dc}$ $\begin{bmatrix} \frac{di_L}{dt} \\ \frac{dV_C}{dt} \end{bmatrix} = \begin{bmatrix} 0 & \frac{-1}{L} \\ \frac{1}{C_{out}} & \frac{-1}{RC_{out}} \end{bmatrix}\begin{bmatrix} i_L \\ V_C \end{bmatrix} + \begin{bmatrix} \frac{D}{L} \\ 0 \end{bmatrix}[V_{in}]$

By substituting Equation (37) into the output equation of the plant is resulted as:

$$Y(s) = \left[C(sI - A)^{-1}B + D\right]U(s) \qquad (38)$$

Transfer function of the system is given by:

$$G(s) = \frac{Y(s)}{U(s)} = C(sI - A)^{-1}B + D \qquad (39)$$

AC small signal analysis of the converters consists of obtaining averaged state-space equation of the converters and superimposing ac variation (perturbation) around the steady-state point. To find the steady-state operating point of the system, time derivative is set to zero in the state equation as shown in Equation (23). Dynamic AC small signal model is given as:

$$\hat{x}(s) = (sI - A)^{-1}\left[(A_1 - A_2)X + (B_1 - B_2)V_{in}\right]\hat{d}(s) \qquad (40)$$

The state variables of the system are inductor current (i_L) and capacitor voltage (V_C) since the inductor and capacitor are the only energy storage elements of the buck converter. Accordingly, the state vector x of the buck converter is:

$$x = \begin{bmatrix} i_L \\ V_C \end{bmatrix} \qquad (41)$$

Analysis of the buck converter in CCM and deriving its averaged state-space equation is given in Table 4.

The state variable vector X at steady-state operation point from Equation (23) can be rewritten by considering that all parasitic resistances are zero as the following:

$$X = -A^{-1}BV_{in} = -\frac{\text{adj}\begin{bmatrix} 0 & \frac{-1}{L} \\ \frac{1}{C_{out}} & \frac{-1}{R_{Load}C_{out}} \end{bmatrix}}{\det\begin{bmatrix} 0 & \frac{-1}{L} \\ \frac{1}{C_{out}} & \frac{-1}{R_{Load}C_{out}} \end{bmatrix}}\begin{bmatrix} \frac{D}{L} \\ 0 \end{bmatrix}V_{in} = \begin{bmatrix} \frac{C_{out}^2 DV_{in}}{R_{Load}} \\ DV_{in} \end{bmatrix} \qquad (42)$$

Substituting Equation (42) and the averaged system and input matrices derived in Table 4 into Equation (40) results in:

$$\frac{\hat{x}(s)}{\hat{d}(s)} = \frac{\begin{bmatrix} \hat{i}_L \\ \hat{V}_C \end{bmatrix}}{\hat{d}(s)} = \begin{bmatrix} \frac{V_{in}\left(C_{out}R_{Load}s + 1\right)}{C_{out}LR_{Load}s^2 + Ls + R_{Load}} \\ \frac{V_{in}R_{Load}}{C_{out}LR_{Load}s^2 + Ls + R_{Load}} \end{bmatrix} \qquad (43)$$

Duty ratio to the inductor current transfer function is obtained from Equation (43) by substitution of the calculated components values for one phase of the intended buck converter as:

$$\frac{i_L(s)}{d(s)} = \frac{V_{in}}{L} \cdot \frac{s + \frac{1}{R_{Load}C_{out}}}{s^2 + \frac{s}{R_{Load}C_{out}} + \frac{1}{LC_{out}}} = (6.1455e4) \cdot \frac{s + 1.6e4}{s^2 + 1600s + 8.0841e7} \tag{44}$$

5 | PROPORTIONAL-INTEGRAL PWM ERROR COMPENSATOR DESIGN

The Proportional-Integral (PI) feedback compensator structure is used in wide range of applications in control systems. The main properties make extensive use of PI controller are its simplicity in implementation, easy comprehension of its impacts on systems and high efficiency. In this paper, PI controllers is designed as a PWM error compensator to provide current balance between phases of the interleaved buck converter. Moreover, robustness of the system that is adversely affected with parameter uncertainty is increased with the use of PI controller. The unity feedback structure of the single-phase proposed PVE system is given in Figure 16.

The closed-loop transfer function of inductor current to the duty ratio for the unity feedback system with PI control is the following:

of the proposed PR-P control structure is done by using comparative analysis evaluation method with widely used PI control structure. Current feedback control structure of the overall system is given in Figure 17.

When designing a controller for a system, open-loop response is considered on a preferential basis to determine what needs to be improved for a desired response. Figure 18 depicts the open-loop and uncontrolled closed-loop step responses of derived transfer function of the PVE.

Figure 19 illustrates the closed-loop step response comparison plot of the derived transfer function of the PVE controlled with the proposed PR-P and PI controllers.

Step response characteristics of the PVE in terms of open-loop and closed-loop is given in Table 6. Time domain analysis of the system regarding transient and steady-state characteristics indicates that enhanced performance outcomes are achieved with the proposed PR-P controller.

$$G_{CL}(s) = \frac{V_{in}K_p}{L} \frac{s^2 + s\left(\frac{1}{CR_{Load}} + \frac{K_i}{K_p}\right) + \frac{K_i}{K_p CR_{Load}}}{s^3 + s^2\left(\frac{1}{CR_{Load}} + \frac{K_p V_{in}}{L}\right) + s\left(\frac{1}{CL} + \frac{K_p V_{in}}{CLR_{Load}} + \frac{K_i V_{in}}{L}\right) + K_i V_{in}} \tag{45}$$

K_p and K_i values are calculated as 0.21 and 709, respectively, according to stability criteria of SMPS given in Table 5.

6 | COMPARATIVE ANALYSIS OF THE PROPOSED PR CONTROLLER

Common goals of control systems are obtaining fast rise time, minimal overshoot, and zero steady-state error. In

A properly designed controller that is perfectly tuned to the model may still be under the risk of reduced performance on the real system. Straightforward approach to overcome this problem is to add margin into the design. Regarding this issue, a consistent system must be designed in such a way to ensure that the stability is exceeded in a certain amount instead of just meeting the desired performance so any deviations on the system dynamics will not affect the requirements. Classical gain and phase margins analysis of a system at some critical frequency
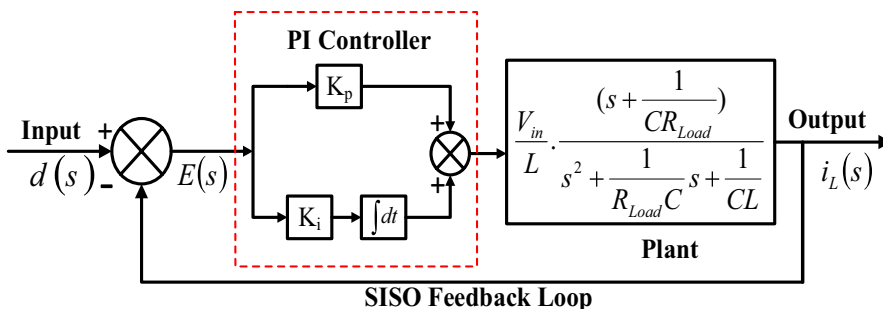

FIGURE 16 The unity feedback control structure of the PVE

TABLE 5 Switch mode power supply stability criteria

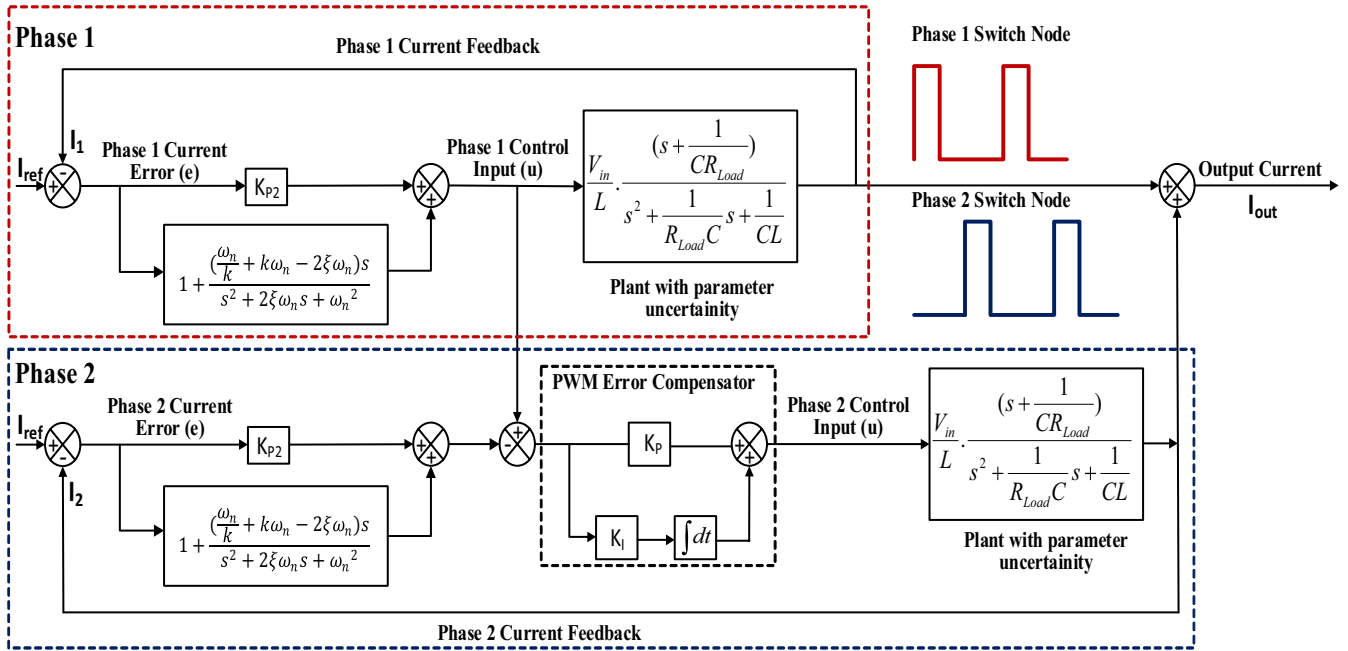| Parameters	Value
Crossover (cutoff frequency)	Between the range of 1/10th to 1/8th of switching frequency
Phase margin	Greater than 45°
Gain margin	Greater than 10 dB
The slope of the gain curve at the crossover frequency	≈ -20 db/decade

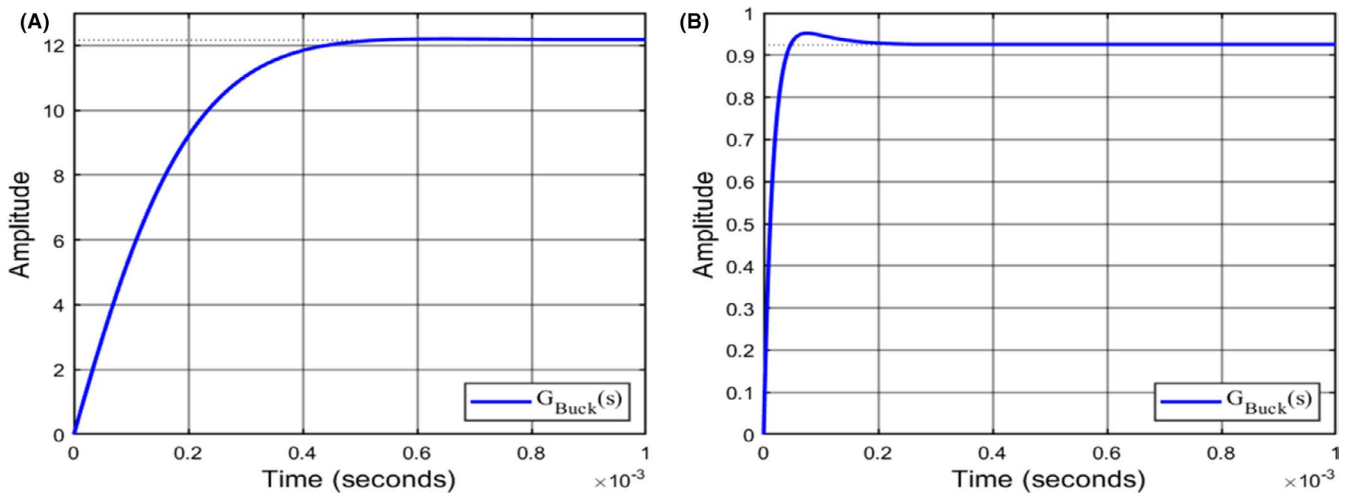**FIGURE 17** Overall system current feedback control structure

FIGURE 18 PVE step response (A) open-loop step response; (B) uncontrolled closed-loop step response

or frequencies is made for the purpose of designing a robust control. The amount of margin chosen for a system depends on uncertainty between the model and the real system. Classical gain and phase margin analysis of a system is one of the assessment methods of its robustness but does not give a complete view about the system robustness since the effects of the gain and phase are assessed individually. Therefore, combination of gain and phase uncertainty needs to be considered. In respect to this, disk margin analysis has to be performed in addition to

individual assessment of the margins with classical approach. The PVE feedback loop with the proposed PR-P controller and uncertain multiplicative factor F that has the nominal value of 1 is given in Figure 20. The system has infinite gain margin, 89.98° phase margin at the gain crossover frequency of 6.2068e+06 rad/s, 25 μs delay margin. Bandwidth of the system is 7.86e + 03 rad/s.

Due to the plant uncertainties and other sources of variations, the loop gain and phase are exposed to fluctuations. The general approaches to determine the amount of uncertainty are either quantifying through experiments or approximation based on gained insight about the system after wide range of simulations. The gain and phase uncertainty analysis in feedback loop will be performed
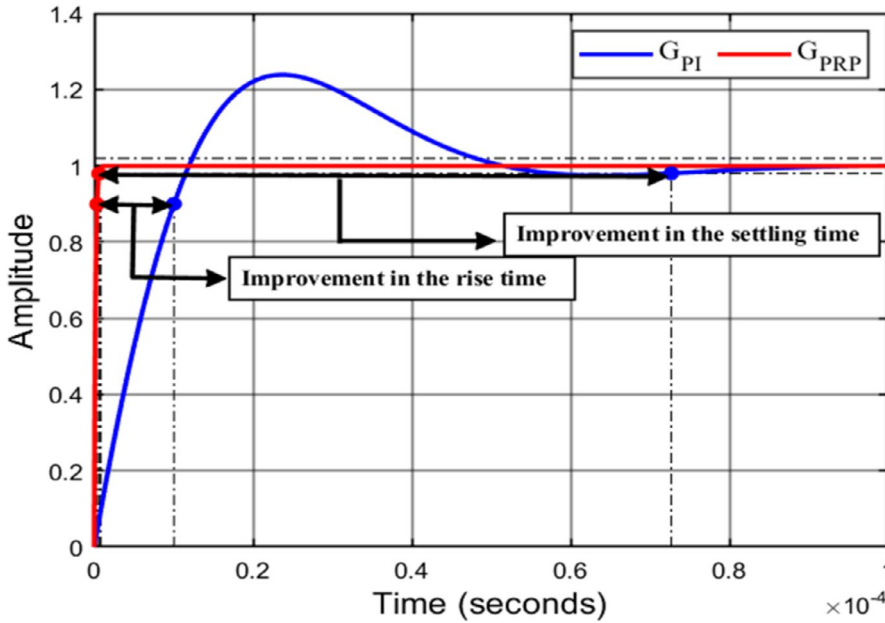

FIGURE 19 PR-P and PI controlled closed-loop step response of the PVE

TABLE 6 Time domain analysis of the overall system

| Step response characteristics	Open-loop	Closed-loop without controller	Closed-loop PI control	Closed-loop PR-P control
Rise time	2.7203e-04	2.8250e-04	9.1876e-06	3.5257e-07
Settling time	4.1803e-04	1.1501e-04	7.2690e-05	6.2230e-07
Settling minimum	10.9681	0.8414	0.9030	0.9002
Settling maximum	12.2004	0.9518	1.2385	0.9992
Overshoot	0.31	3.0028	23.8460	5.8370e-04
Undershoot	0	0	0	0
Peak	12.2004	0.9518	1.2385	0.9992
Peak time	6.5048e-04	7.5723e-05	2.3304e-05	1.1058e-06
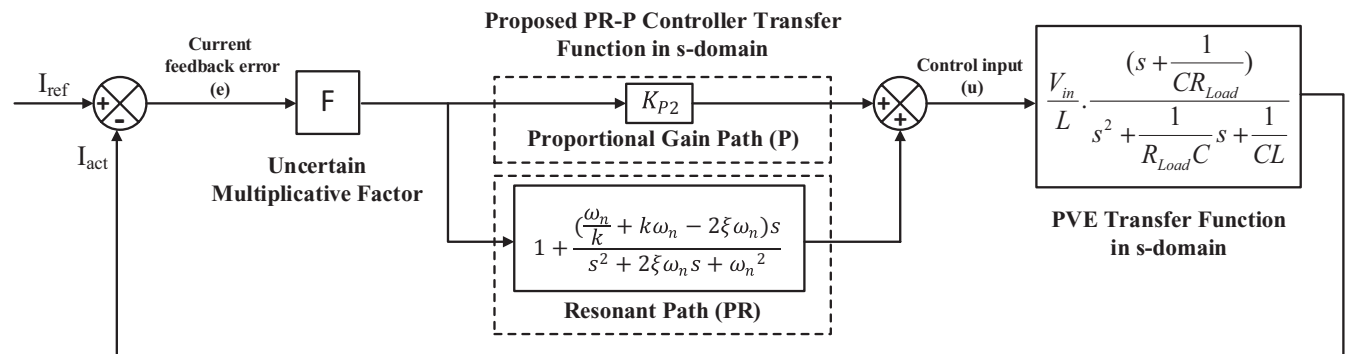
FIGURE 20 The PVE feedback loop with the proposed PR-P controller and multiplicative factor F

FIGURE 21 Specified range of gain/phase variations and multiplicative factor *F*
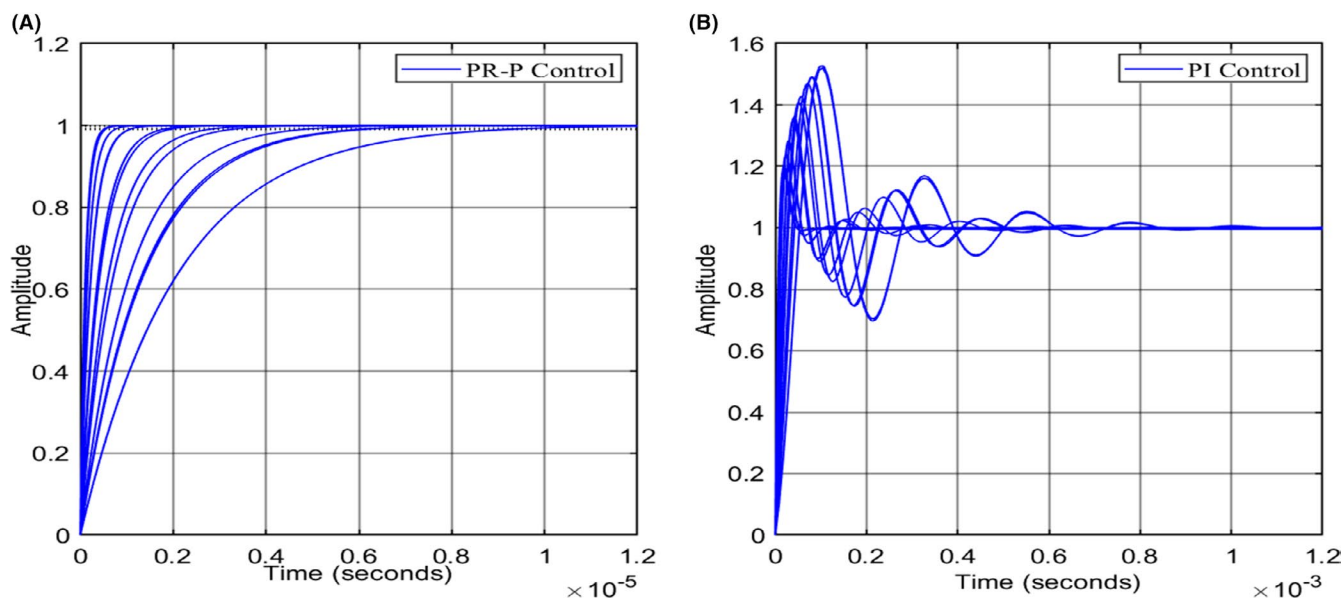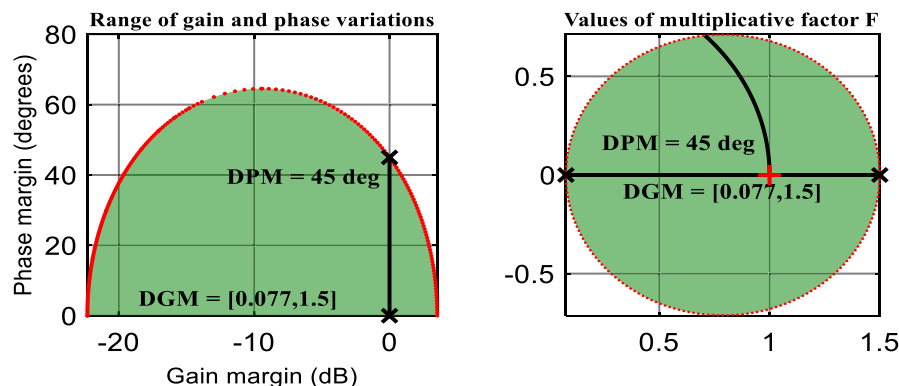

FIGURE 22 Closed-loop step response of the PVE for the set of values *F* (A) with PR-P control; (B) with PI control

based on to the stability criteria given in Table 5. It is supposed that the open-loop gain variation is 50% (increase or decrease), and the phase variation is $\pm 45°$. The set of values *F* that captures the uncertain gain/phase with relative gain change in [0.0765, 1.5] and phase change of $\pm 45°$ is given in Figure 21.

The Figure 21 shows that the gain can vary between 7% and 150% of its nominal value without of phase variation and the phase can vary by $\pm 45°$ without gain variation. In case of variation for both gain and phase, their deviation remains inside the shaded region in the left. The step response of incorporating of this uncertainty into the closed-loop model is given in Figure 22.

The robust stability margin of the system that is full range of simultaneous gain and phase variations tolerable by the closed-loop system is obtained as.

The closed-loop step response indicates that the system performs well and yields good robustness to specified gain and phase variations. The robust stability margin of the PR-P controlled system is 100% that means feedback loop can withstand 100% of the specified uncertainty generated

by *F*. Figure 23A shows that 100% uncertainty specified in *F* therefore in the open loop system amounts the gain variation between 0.6% and 150% of the nominal value, and phase variation of $\pm 49°$. The robust stability margin of the PI controlled system is 87%, meaning that feedback loop can withstand only 87% of the specified uncertainty. Figure 23B indicates that 87% uncertainty specified in *F* therefore in the open loop system amounts the gain variation between 24% and 140% of the nominal value, and phase variation of $\pm 37°$. The proposed PR-P and PI current waveform control of single-phase PVE for varying irradiance of 1000, 800, and 600 W/m^2 that correspond to 7.3483 A, 5.8656 A, and 4.4153 A, respectively, and voltage outputs for both control configurations are given in Figure 24. The proposed PR-P controller structure for the PVE reveals better performance than PI control in terms of transient response and reduction in the current and voltage ripples. While the system reaches steady state in less than 1 millisecond for PI control, 10 times faster convergence to steady state is attained with the proposed PR-P controller.
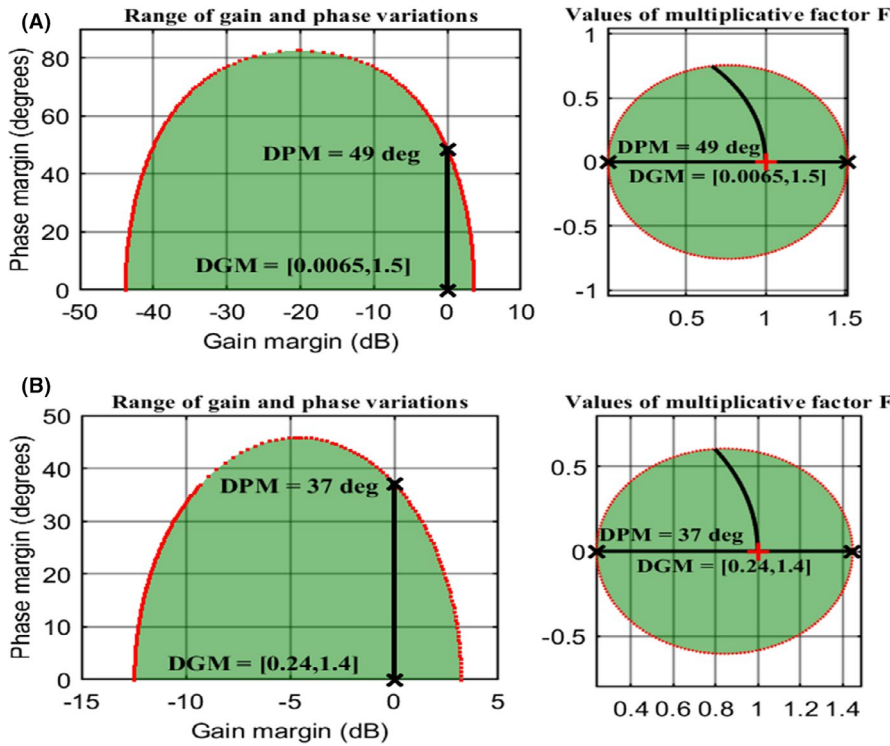
—

FIGURE 23 The gain/phase variations tolerable (robust stability margin) by the closed-loop system (A) PR-P control; (B) PI control
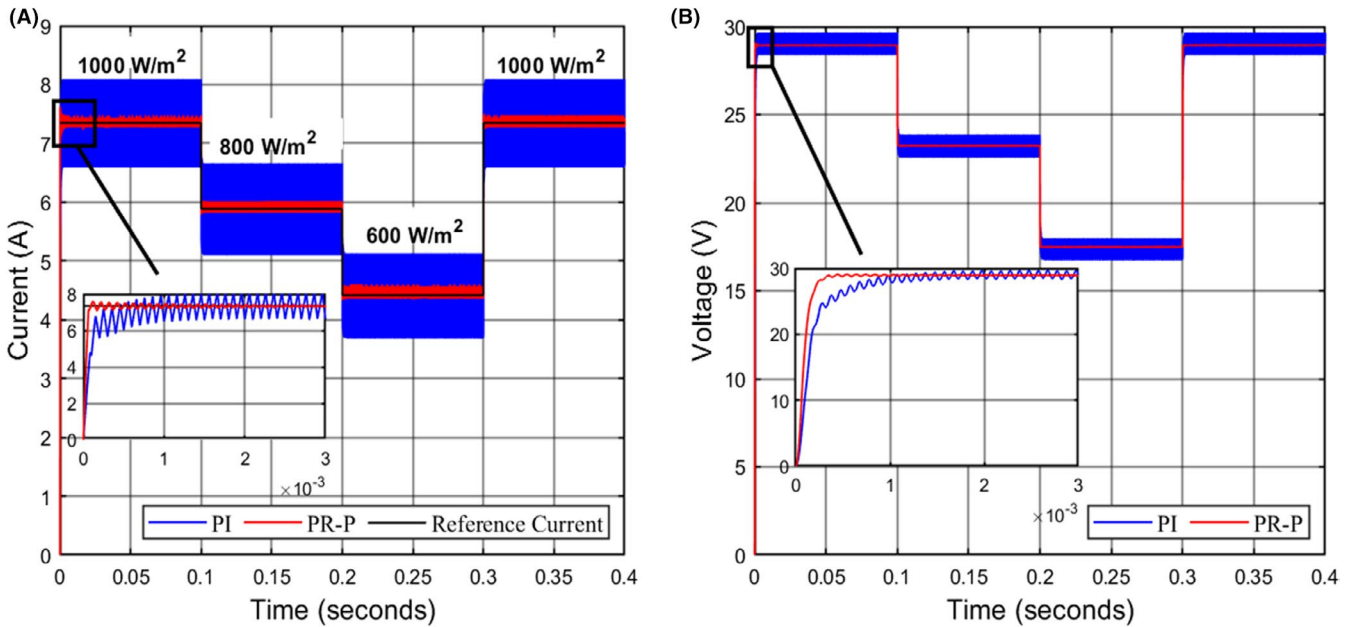

FIGURE 24 Output current and voltage waveforms of PR-P and PI controlled single-phase PVE

Figure 25 shows that phase currents are accurately balanced for varying irradiance conditions for interleaved buck converter-based PVE. Furthermore, the output current ripples are reduced compared to single-phase buck converter-based PVE given in Figure 24.

Figure 26 displays the performance of the PVE to variations in the values of the inductance in each phase at different irradiance values. In Figure 26A, the inductance of each phase is halved and additionally 20% inductance difference is applied between phases. In

Figure 26B, additional dissimilarity is implemented in terms of DC parasitic resistance of the inductor. The value of parasitic resistance is set to 2 and 2.4 Ω (20% variance) for phases. Parameter uncertainties and variations in component values are inevitable in dynamics systems. The objective PVE system reveals good performance with the proposed PR-P controller under parameter variations.

Figure 27 displays the PVE and the emulated PV module I-V characteristics curves at different irradiance

FIGURE 25 Output current waveform of PR-P controlled interleaved buck converter-based PVE
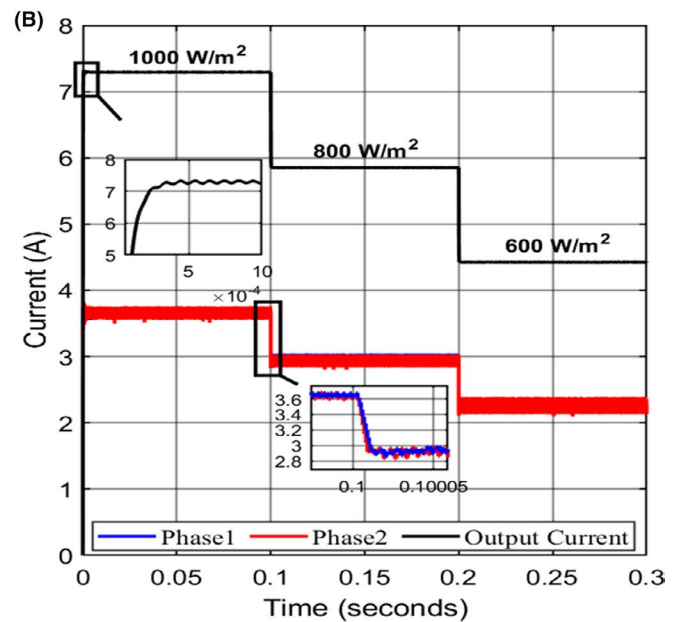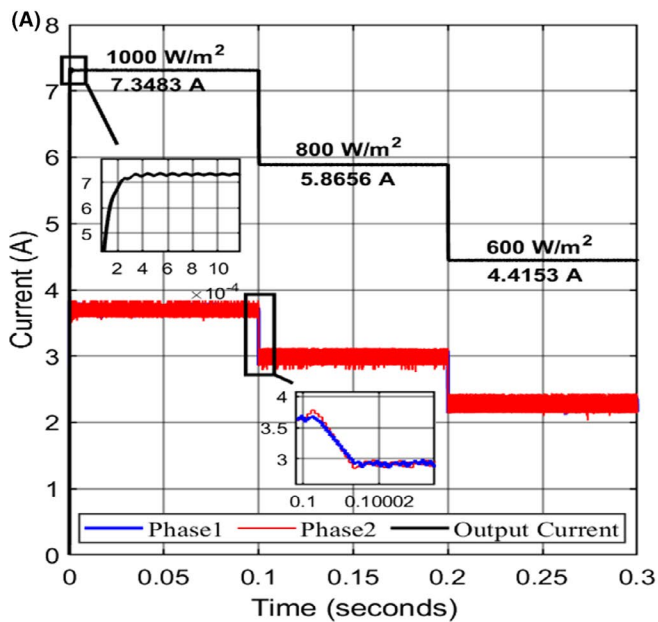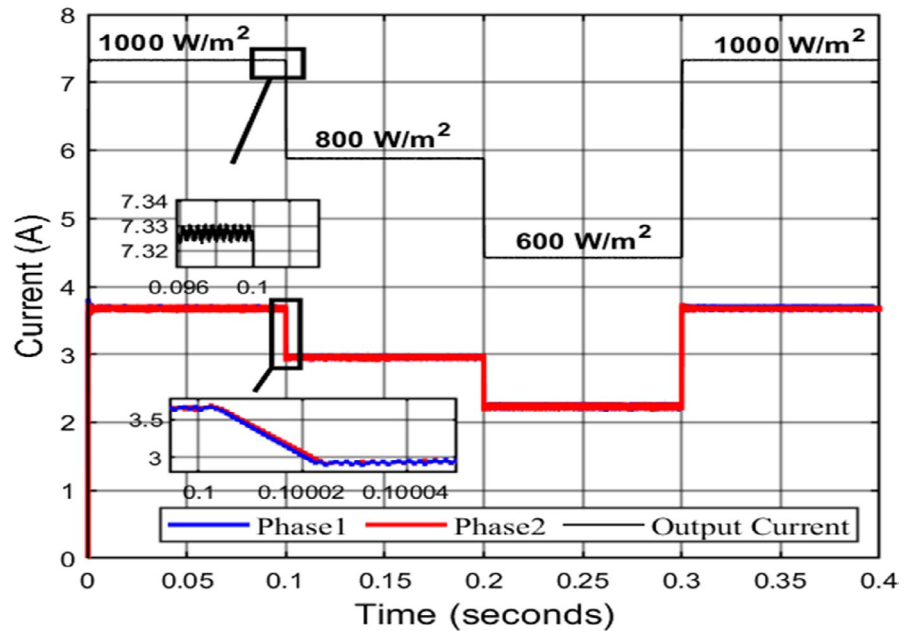

FIGURE 26 Output current waveforms under variations of inductance and DC parasitic resistance (A) $L_1 = (7.8108e\text{-}04) \times 50\%$ H, $L_2 = (7.8108e\text{-}04) \times 40\%$ H; (B) $L_1 = (7.8108e\text{-}04) \times 50\%$ H, $L_{R1} = 2\ \Omega$, $L_2 = (7.8108e\text{-}04) \times 40\%$ H, $L_{R2} = 2.4\ \Omega$

values. The proposed PR-P controller interleaved buck converter-based PVE system I-V curves correspond to the parameters of the emulated PV module (1Soltech 1STH-215-P) given in Table 2 and I-V curves given in Figure 14.

7 | CONCLUSION

This paper has presented interleaved buck converter-based photovoltaic emulator current control with proportional-resonant-proportional (PR-P) controller.

By considering the most commonly used controller mappings for SMPS with their features, advantages, and limitations, verification and validation of the designed PR-P controller compared with the PI controller have been presented to illustrate the proposed controller scheme efficiency by using robust control theory. Unlike the classical gain and phase margin analysis of the system through which effects of the gain and phase are worked individually for the assessment of its robustness, combination of gain and phase uncertainty has been considered in the paper. In respect to this, disk margin analysis has been performed in addition
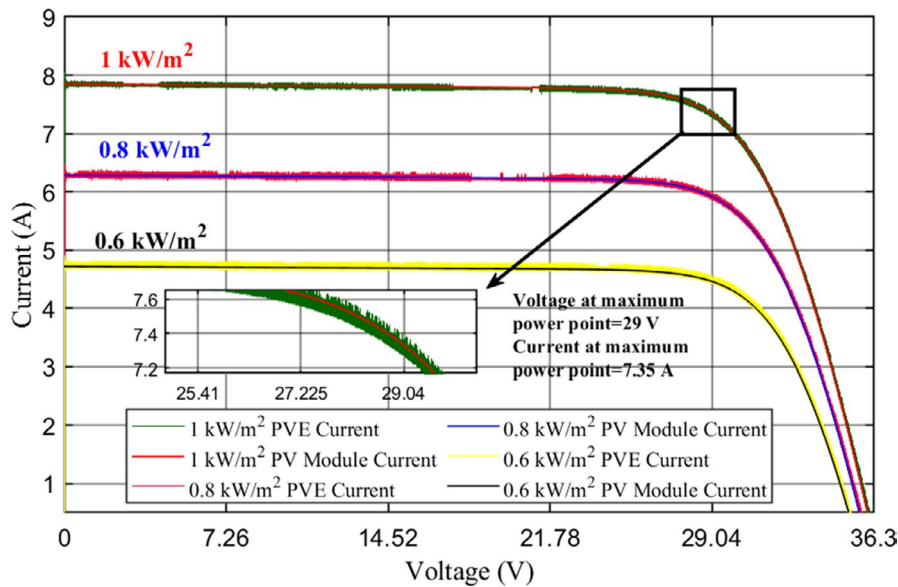
FIGURE 27 I-V characteristics curves at different irradiance values for PVE and PV module

to straightforward classical approach (individual gain and phase margins assessment) to overcome the main issues in control systems designing such as complex dynamics, uncertainty, intentional simplicity, stochastic events, and process variations. The stability of a closed-loop system against gain or phase fluctuations in the open-loop response has been measured by disk margins. The implementation has been carried out by adding multiplicative uncertainty factor F with the nominal value of 1 to the buck converter-based PVE feedback loop. Since the disk margin is a metric that indicates how much uncertainty the loop can withstand before becoming unstable, 50% (increase or decrease) open-loop gain and $\pm45°$ phase variation has been added into the system by setting the values of F. The results have revealed that 13% improvement in the robust stability margin and 12° bigger phase toleration with the PR-P controller have been achieved. Additionally, the proposed controller has shown superior performance in terms of 10 times faster-converging transient response, zero steady-state error, significant reduction in current ripple and properly functioning with parameters uncertainty (highly robust) that constitutes primary concern in multiphase converters' load sharing. Moreover, unconventional design process of the controller reduces the computational complexity, provides cost-effectiveness and simple implementation. Output voltage and current waveforms produced by the PVE at different irradiance values reflects the I-V characteristics curves of the emulated PV panel accurately.

ACKNOWLEDGMENTS

ORCID

Cagfer Yanarates https://orcid.org/0000-0003-0661-0654

REFERENCES

1. Höök M., Tang X. Depletion of fossil fuels and anthropogenic climate change—A review. *Energy Policy*. 2013;52:797–809. doi:10.1016/j.enpol.2012.10.046
2. MacKay DJ. *Sustainable Energy-Without The Hot Air*. UIT Cambridge Ltd.; 2012.
3. Shahabuddin M, Riyaz A, Asim M, Shadab MM, Sarwar A, Anees A. Performance based analysis of solar PV emulators: a review. *2018 Int. Conf. Comput. Charact. Tech. Eng. Sci. CCTES 2018*, 2019;94-99.
4. Shrestha NK, Wang J. Water quality management of a cold climate region watershed in changing climate. *J Environ Informatics*. 2020;35(1):56-80.
5. Ullah N, Nisar F, Alahmadi AA. Closed loop control of photo voltaic emulator using fractional calculus. *IEEE Access*. 2020;8:28880-28887.
6. Ram JP, Manghani H, Pillai DS, et al. Analysis on solar PV emulators: a review. *Renew Sustain Energy Rev*. 2018;81:149-160.
7. Moussa I, Khedher A. Photovoltaic emulator based on PV simulator RT implementation using XSG tools for an FPGA control: theory and experimentation. *Int Trans Electr Energy Syst*. 2019;29(8):1-16.
8. Ji L, Huang GH, Niu DX, Cai YP, Yin JG. A stochastic optimization model for carbon-emission reduction investment and sustainable energy planning under cost-risk control. *J Environ Informatics*. 2020;36(2):107-118.
9. John Twidell TW. *Renewable Energy Resources*, 3rd edn. Routledge, Taylor&Francis Group, 2015.
10. Haque A, Zaheeruddin. Research on solar photovoltaic (PV) energy conversion system: an overview. *IET Conference Publications*. 2013;605-611.
11. Prasad AR, Singh S, Nagar H. Importance of solar energy technologies for development of rural area in India. no. July, 2017.
12. Kabir E, Kumar P, Kumar S, Adelodun AA, Kim KH. Solar energy: potential and future prospects. *Renew Sustain Energy Rev*. 2018;82:894-900.

13. Shaikh MRS. A review paper on electricity generation from solar energy. *Int J Res Appl Sci Eng Technol.* 2017;V(IX):1884-1889.

14. González-Medina R, Patrao I, Garcerá G, Figueres E. A low-cost photovoltaic emulator for static and dynamic evaluation of photovoltaic power converters and facilities. *Prog Photovoltaics Res Appl.* 2014;22(2):227-241. doi:10.1002/pip.2243

15. Ayop R, Tan CW. Rapid prototyping of photovoltaic emulator using buck converter based on fast convergence resistance feedback method. *IEEE Trans Power Electron.* 2019;34(9):8715-8723.

16. Moussa I, Khedher A, Bouallegue A. Design of a low-cost PV emulator applied for PVECS. *Electronics.* 2019;8(2):232.

17. Zhou Z, Holland PM, Igic P. MPPT algorithm test on a photovoltaic emulating system constructed by a DC power supply and an indoor solar panel. *Energy Convers Manag.* 2014;85:460-469.

18. Garg P, Priyanshi, Bhuvaneswari G. Power electronic circuit based implementation of a solar PV emulator using a power factor corrected buck converter. *2018 IEEMA Eng Infin Conf eTechNxT.* 2018;1-6.

19. Yanarates C, Wang Y, Zhou Z. Unity proportional gain resonant and gain scheduled proportional (PR-P) controller-based variable perturbation size real-time adaptive perturb and observe (P & O) MPPT algorithm for PV systems. *IEEE Access.* 2021;9:138468-138482.

20. Jayawardana I, Man Ho CN, Pokharel M. Design and implementation of switch-mode solar photovoltaic emulator using power-hardware-in-the-loop simulations for grid integration studies. *2019 IEEE Energy Convers Congr Expo ECCE.* 2019;889-894.

21. González-Medina R., Patrao I., Garcerá G., Figueres E. A low-cost photovoltaic emulator for static and dynamic evaluation of photovoltaic power converters and facilities. *Progress in Photovoltaics: Research and Applications.* 2014;22(2):227–241. doi:10.1002/pip.2243

22. Azharuddin SM, et al. A near accurate solar PV emulator using dSPACE controller for real-time control. *Energy Procedia.* 2014;61:2640-2648.

23. Ibrahim H, Anani N. Variations of PV module parameters with irradiance and temperature. *Energy Procedia.* 2017;134:276-285.

24. Parisi C. Multiphase Buck Design From Start to Finish (Part 1), no. May; 2019:1-20. www.ti.com

25. Baba D. Benefits of a multiphase buck converter. *Texas Instruments*, no. 1, pp. 8–13, 2012. www.ti.com

26. Kanzian M, Gietler H, Agostinelli M, Priewasser R, Huemer M. Vergleichsstudie digitaler Regelkonzepte für mehrphasige Abwärtswandler. *Elektrotechnik und Informationstechnik.* 2018;135(1):54-60.

27. Lin JT, Hu KY, Tsai CH. Digital multiphase buck converter with current balance/phase shedding control. IEEE Reg. 10 Annu. Int. Conf. Proceedings/TENCON, vol. 2016-Janua, pp. 5-9, 2016.

28. Silva L, Mendes V, Seleme SI, Cousineau M. Distributed control for the current balancing of a multiphase converter using a single voltage sensor. *PCIM Eur. Digit. days 2021; Int. Exhib. Conf. Power Electron. Intell. Motion, Renew. Energy Energy Manag.*, no. May, pp. 1-7, 2021.

29. Yuan Z, Wen P, Xu H, Yuan Z. Multi-loop current control strategy based on predictive control for multiphase pulse power supplies. *J Power Electron.* 2021;21(3):553-562.

30. Xu Q, Vafamand N, Chen L, Dragicevic T, Xie L, Blaabjerg F. Review on advanced control technologies for bidirectional DC/DC converters in DC microgrids. *IEEE J Emerg Sel Top Power Electron.* 2021;9(2):1205-1221.

31. Nikhar AR, Apte SM, Somalwar R. Review of various control techniques for DC-DC interleaved boost converters. *Proc - Int Conf Glob Trends Signal Process Inf Comput Commun ICGTSPICC 2016.* 2017;432-437.

32. Adnan MF, Oninda MAM, Nishat Mirza Muntasir, Islam Nafiul. Design and simulation of a DC - DC boost converter with PID controller for enhanced performance. *Int J Eng Res.* 2017;6(9).

33. Hekimoğlu B, Ekinci S, Kaya S. Optimal PID controller design of DC-DC buck converter using whale optimization algorithm. *2018 Int. Conf. Artif. Intell. Data Process. IDAP 2018*, no. September 2018, 2019.

34. Mumtaz F, Zaihar Yahaya N, Tanzim Meraj S, Singh B, Kannan R, Ibrahim O. Sliding mode control and chattering : the concept. *Ain Shams Eng. J.*, no. xxxx, 2021.

35. Utkin V, Poznyak A, Orlov Y, Polyakov A. Conventional and high order sliding mode control. *J Franklin Inst.* 2020;357(15):10244-10261.

36. Fatoorehchi H, Ghorbanian SA. Sliding mode control for heartbeat electrocardiogram tracking problem. *J Chem Petroleum Eng.* 2019;53(2):265-272.

37. Zaihidee FM, Mekhilef S, Mubin M. Robust speed control of PMSM using sliding mode control (SMC)—a review. *Energies.* 2019;12(9).

38. Augustine M. Sliding mode control and chattering : the concept. no. March, 2019.

39. Wei Q, Wu B, Xu D, Zargari NR. Model predictive control of capacitor voltage balancing for cascaded modular DC-DC converters. *IEEE Trans Power Electron.* 2017;32(1):752-761.

40. An F, Song W, Yang K, Hou N, Ma J. Improved dynamic performance of dual active bridge dc-dc converters using MPC scheme. *IET Power Electron.* 2018;11(11):1756-1765.

41. Irmak E, Güler N. A model predictive control-based hybrid MPPT method for boost converters. *Int J Electron.* 2020;107(1):1-16.

42. Ibrahim O, Yahaya NZ, Saad N. State-space modelling and digital controller design for DC-DC converter. *Telkomnika (Telecommunication Comput Electron Control.* 2016;14(2):497-506.

43. Tahir S, Wang J, Baloch MH, Kaloi GS. Digital control techniques based on voltage source inverters in renewable energy applications: a review. *Electron.* 2018;7(2).

44. Freytes J, Bergna G, Are Suul J, D'Arco S, Saad H, Guillaud X. State-space modelling with steady-state time invariant representation of energy based controllers for modular multi-level converters. *2017 IEEE Manchester PowerTech, Powertech.* 2017;2(2):1-7.

45. Azer P, Emadi A. Generalized state space average model for multi-phase interleaved buck, boost and buck-boost DC-DC converters: Transient, steady-state and switching dynamics. *IEEE Access.* 2020;8:77735-77745.

46. Tarbosh QA, et al. Review and investigation of simplified rules fuzzy logic speed controller of high performance induction motor drives. *IEEE Access.* 2020;8:49377-49394.

47. Araria R, Berkani A, Negadi K, Marignetti F, Boudiaf M. Performance analysis of DC-DC converter and DTC based

fuzzy logic control for power management in electric vehicle application. *J Eur Des Syst Autom*. 2020;53(1):1-9.

48. Soliman MA, Hasanien HM, Azazi HZ, El-Kholy EE, Mahmoud SA. An adaptive fuzzy logic control strategy for performance enhancement of a grid-connected PMSG-Based wind turbine. *IEEE Trans Ind Informatics*. 2019;15(6):3163-3173.

49. Santos N, Silva JF, Soares V. Control of single-phase electrolytic capacitor-less isolated converter for DC low voltage residential networks. *Electron*. 2020;9(9):1-19.

50. Yanarates C, Zhou Z. Symmetrical pole placement method-based unity proportional gain resonant and gain scheduled proportional (PR-P) controller with harmonic compensator for single phase grid-connected PV inverters. *IEEE Access*. 2021;9:93165-93181.

51. Khomsi C, Bouzid M, Jelassi K, Champenois G. Harmonic current compensation in a single-phase grid connected photovoltaic system supplying nonlinear load. 2018 9th Int. Renew. Energy Congr. IREC. 2018;2018(March):1-6.

52. Parvez M, Elias MFM, Rahim NA. Performance analysis of PR current controller for single-phase inverters. *IET Conf Publ*. 2016;2016(CP688):1-8.

53. Zammit D, Spiteri Staines C, Apap M, Licari J. Design of PR current control with selective harmonic compensators using Matlab. *J Electr Syst Inf Technol*. 2017;4(3):347-358.

54. Lu W, Qu X, Ma J. Auxiliary bridge arm–based switching control for optimal unloading transient performance of multiphase buck converters. *Int J Circuit Theory Appl*. 2020;48(6):919-933.

55. Yang K, Wu G, Zhang X. The control technology of BUCK converter. *Appl Mech Mater*. 2012;150:240-244.

56. Rowell D. State-space representation of LTI systems. http://web.mit.edu/2.14/www/Handouts/StateSpace.pdf, no. October, 2002, pp. 1–18.

57. Herbst G. A building-block approach to state-space modeling of DC-DC converter systems. *J*. 2019;2(3):247-267.

58. Polivka WM, Chetty PRK, Middlebrook RD. State-Space Average modelling of converters with parasitics and storage-time modulation. *PESC Rec - IEEE Annu Power Electron Spec Conf*. 1980;1980:119-143.

59. Suman G, Kumar BVSP, Kumar MS, Babu BC, Subhashini KR. Modeling, analysis and design of synchronous buck converter using state space averaging technique for PV energy system. *Proc. - 2012 Int. Symp. Electron. Syst. Des. ISED 2012*, pp. 281-285, 2012.